PHYSICAL REVIEW B **99**, 165417 (2019)

Enhanced discretization of surface integral equations for resonant scattering analysis of sharp-edged plasmonic nanoparticles

Ivan Sekulic,[1,*] Dimitrios C. Tzarouchis,[2] Pasi Ylä-Oijala,[2] Eduard Ubeda,[1] and Juan M. Rius[1]
[1]*CommSensLab, Universitat Politecnica de Catalunya (BarcelonaTech), Jordi Girona 1-3, 08034 Barcelona, Spain*
[2]*Department of Electronics and Nanoengineering, Aalto University, P.O. Box 15500, FI-00076 Aalto, Finland*

(Received 5 December 2018; published 10 April 2019)

The surface integral equation (SIE) method, discretized with the method of moments, is a well-established methodology for the scattering analysis of subwavelength plasmonic nanoparticles. SIEs are usually discretized with low-order basis functions that preserve the normal continuity of the surface currents across the edges arising in the meshed boundary, such as Rao-Wilton-Glisson (RWG) functions. However, the plasmonic enhancement modeling on sharp-edged particles is an extremely challenging task, especially due to the singular fields exerted at sharp corners, exposing a slow (or no) convergence in the computation of the scattering and absorption spectra. In this paper, we propose an alternative discretization strategy based on a discontinuous basis function set in conjunction with a volumetric-tetrahedral testing scheme. We demonstrate the potential of the proposed discretization scheme by studying scattering and absorption spectra of three canonical plasmonic polyhedra, i.e., a hexahedral, an octahedral, and a tetrahedral silver inclusion. The results expose an improved accuracy and faster convergence in both far-field and near-field regions when compared to the standard RWG implementation. The proposed discretization scheme can offer faster and more accurate routes towards the exploration and design of the plasmonic resonant spectrum of sharp-edged nanoparticles and nanoantennas.

DOI: 10.1103/PhysRevB.99.165417

I. INTRODUCTION

When metallic nanoscale particles are excited with electromagnetic fields at optical frequencies, localized free-charge oscillations, known as localized surface plasmons, are induced on metal interfaces [1]. Plasmonic effects at the nanoscale are especially interesting because they produce strong near-field enhancement giving rise to new interesting applications in photovoltaic systems, waveguiding, optical metamaterials, nanoantennas, photodetectors, and nonlinear optics [2–10]. Therefore, efficient and accurate electromagnetic modeling of these phenomena is called for.

Among the plethora of numerical methods available for the analysis of plasmonic nanostructures, such as the discrete dipole approximation (DDA) [11–13] and the finite difference time domain (FDTD) [14] method, the surface integral equation (SIE) approach, sometimes alternatively called the boundary element method, is particularly attractive for open-region (scattering) problems and for problems in which the important physical phenomena take place close to the boundaries. In that method, both the unknowns and the analysis lie on the interfaces between different homogeneous regions and the radiation condition at infinity is inherently satisfied [15–17]. At lower frequencies (radio or microwave frequencies) metals can be well approximated as perfect electric conductors (PECs). In the optical regime, however, the penetration of the fields into the particle and the plasmonic effects have to be accurately taken into account.

For penetrable objects, SIEs can be expressed in many alternative forms. One of the most popular formulations is the PMCHWT (Poggio-Miller-Chang-Harrington-Wu-Tsai) integral equation formulation [18–20], recently applied widely also in the analysis of nanoplasmonic systems [21–23]. In the standard Galerkin method of moments (MoM) discretization of the PMCHWT equations [24], where the current expansion (basis) functions are identical to field-testing functions, the unknown equivalent electric and magnetic surface current densities are expanded with the Rao-Wilton-Glisson (RWG) basis functions [25]. These basis functions are associated with mesh edges, straddling two edge-adjacent triangles. They provide a linear approximation of the unknown surface current density inside each triangular facet and guarantee the normal-continuity across adjacent mesh elements; whereby they represent a low-order set of basis functions. RWG basis functions are *divergence-conforming*, since they span a finite-dimensional subspace inside vector Sobolev divergence space of fractional order, which represents the mathematical space of electric and magnetic surface currents. The discretized equations are cast into matrix form by means of testing the tangential field components with the same set of functions. This discretization of PMCHWT equations is *conforming* with respect to the aforementioned vector Sobolev space mappings, hence providing converging solutions within these spaces as the number of degrees of freedom is increased [26,27].

However, the RWG-PMCHWT scheme is no panacea. Recent advances in nanofabrication have allowed the manipulation of the shape of nanoparticles up to the subnanometer scale [28–31] introducing atomically sharp tips around which electromagnetic energy can be successfully confined (so-called "hot spots") [32]. Therefore, the accurate modeling of the singular field quantities induced around abrupt geometrical

---

[*] ivan.sekulic@tsc.upc.edu

singularities is of great importance [33–36]. Unfortunately, standard divergence-conforming bases, including the higher-order versions, have difficulties in modeling this phenomenon efficiently [37]. In turn, slow convergence in the scattering and absorption spectra in the resonance domain has been reported with respect to the number of degrees of freedom [21,36]. It is clear that a better representation of the singular field quantities is needed. Singular higher-order divergence-conforming bases of the additive kind proposed by Graglia and Lombardi [37] are constructed for this purpose. In addition to the regular divergence-conforming subset, they incorporate the *Meixner* subset [38] in order to capture the singular behavior of currents and charges near sharp corners better. However, these bases have been applied to PEC objects only. Furthermore, the coefficients of the singular terms have to be known *a priori*, and they directly depend on the angle and the material properties of the associated wedge.

Recently, the discretization of the PMCHWT integral equation formulation with facet-based monopolar-RWG basis functions, discontinuous across edges, in conjunction with volumetric-tetrahedral testing has been introduced [39]. These basis functions are identified with facets originating from the surface tessellation and the corresponding discretization scheme is *nonconforming* to the natural divergence function spaces. Despite that, it has been shown by several examples that the monopolar-RWG discretization of PMCHWT equations produces more accurate results in the near field and far field than the standard RWG approach for the cases of dielectric objects that exhibit singular or near-singular field distribution near sharp edges [40]. Unfortunately, the improved performance of the monopolar-RWG PMCHWT approach was observed for a restricted range of heights of the tetrahedral-testing elements [40,41]. A remedy to this problem was given in [41] where a hierarchical decomposition of the monopolar-RWG space is proposed. Although this discretization scheme is edge-based (the basis functions are associated with edges arising in the surface mesh), wider ranges of testing-element heights with improved accuracy have been noticed when compared to the monopolar-RWG PMCHWT technique [41]. So far, the performance of this nonconforming PMCHWT formulation has been tested on subwavelength canonical sharp-edged ferromagnetic targets out of the resonance domain [41]. The improvement in the far-field accuracy, when compared to the standard RWG approach with the same number of unknowns, was attributed to the better singular field modeling near sharp edges.

In this paper, we focus on the scattering analysis of subwavelength sharp-edged plasmonic nanoparticles in the resonance domain. We show with several numerical examples, including hexahedral, octahedral, or tetrahedral silver inclusions, that better convergence in the scattering and absorption spectra with the proposed nonconforming PMCHWT implementation is achieved compared to the standard RWG-PMCHWT technique. Also, we show improved near-field results for the case of a hexahedral silver inclusion computed with our nonconforming implementation and compared to the RWG discretization. The convergence of the resonances of sharp-vertex particles is a particularly interesting example of plasmonic enhancement with a long history [42] used as a test bed for current physics and application-oriented plasmonic research [43–50]. Moreover, the presented methodology could be extended for cases, such as subnano particles and gaps, where enhanced quantum phenomena affect the observed spectrum requiring quantum-corrected classical approaches [51].

II. MATHEMATICAL FORMULATION

A. Surface integral equation formulation of the problem

Consider an arbitrarily shaped plasmonic nanoparticle with orientable surface ($\partial\Omega$) and electromagnetic parameters (ϵ_2, μ_2) embedded in a surrounding medium (usually free space) with parameters (ϵ_1, μ_1). In this work, we assume that the particles are made of silver and modeled according to the Drude model [52]

$$\epsilon_2(\lambda) = \epsilon_0\epsilon_{\mathrm{Ag}}(\lambda) = \epsilon_0\left(\epsilon_\infty - \frac{(\lambda/\lambda_p)^2}{1 - j\lambda/\lambda_d}\right), \tag{1}$$

where $\epsilon_\infty = 5.5$, $\lambda_p = 130$ nm, $\lambda_d = 30\ \mu$m, and ϵ_0 is the electric permittivity of vacuum. The time-harmonic incident electromagnetic field ($\boldsymbol{E}^{\mathrm{inc}}, \boldsymbol{H}^{\mathrm{inc}}$) with angular frequency ω is impinging upon the particle, and time dependency $e^{j\omega t}$ for the fields and currents is assumed and suppressed throughout the paper. The total fields in the region Ω_i, outside ($i = 1$) or inside ($i = 2$) the particle, ($\boldsymbol{E}_i, \boldsymbol{H}_i$), are the sum of the incident fields generated in region Ω_1 and the scattered fields ($\boldsymbol{E}_i^s, \boldsymbol{H}_i^s$) which in turn are generated by equivalent electric and magnetic surface currents $\boldsymbol{J}_i = \hat{\boldsymbol{n}}_i \times \boldsymbol{H}_i$ and $\boldsymbol{M}_i = -\hat{\boldsymbol{n}}_i \times \boldsymbol{E}_i$ residing on the boundary-surface ($\partial\Omega$) inside region Ω_i (see Fig. 1). Here $\hat{\boldsymbol{n}}_i$ is the unit normal vector of $\partial\Omega$ pointing into region Ω_i. According to the equivalence theorem, total fields, $\boldsymbol{E}_i$ and $\boldsymbol{H}_i$, are zero in the equivalent problem outside the respective regions.

Mathematically this surface equivalence principle can be formulated as follows:

$$\delta_{i1}\boldsymbol{E}_i^{\mathrm{inc}}(\boldsymbol{r}) + \eta_i\boldsymbol{\mathcal{T}}^i[\boldsymbol{J}_i](\boldsymbol{r}) - \boldsymbol{\mathcal{K}}^i[\boldsymbol{M}_i](\boldsymbol{r}) = \begin{cases} \boldsymbol{E}_i(\boldsymbol{r}), & \boldsymbol{r} \in \Omega_i, \\ 0, & \boldsymbol{r} \in \Omega_i^c, \end{cases} \tag{2}$$

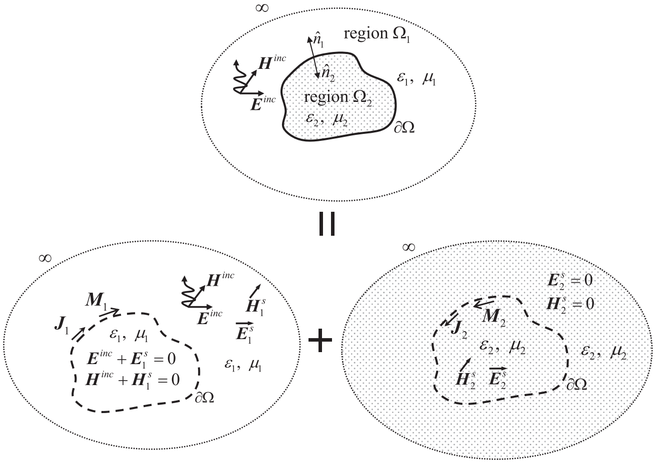

FIG. 1. Schematic representation of the surface equivalence theorem for the case of a single penetrable object.

$$\delta_{i1}\boldsymbol{H}_i^{\mathrm{inc}}(\boldsymbol{r}) + \frac{1}{\eta_i}\mathcal{T}^i[\boldsymbol{M}_i](\boldsymbol{r}) + \mathcal{K}^i[\boldsymbol{J}_i](\boldsymbol{r}) = \begin{cases} \boldsymbol{H}_i(\boldsymbol{r}), & \boldsymbol{r} \in \Omega_i, \\ 0, & \boldsymbol{r} \in \Omega_i^c, \end{cases} \tag{3}$$

with $\delta_{i1} = 1$ if $i = 1$, $\delta_{i1} = 0$ if $i = 2$. The impedance of medium i, occupying region i, is $\eta_i = \sqrt{\mu_i/\epsilon_i}$, and the surface integral operators in (2) and (3) are

$$\mathcal{T}^i[\boldsymbol{F}_i](\boldsymbol{r}) = \frac{1}{jk_i}\nabla\nabla\cdot\int_{\partial\Omega} G_i(\boldsymbol{r},\boldsymbol{r}')\boldsymbol{F}_i(\boldsymbol{r}')\,dS' - jk_i\int_{\partial\Omega} G_i(\boldsymbol{r},\boldsymbol{r}')\boldsymbol{F}_i(\boldsymbol{r}')\,dS', \tag{4}$$

$$\mathcal{K}^i[\boldsymbol{F}_i](\boldsymbol{r}) = \nabla\times\int_{\partial\Omega} G_i(\boldsymbol{r},\boldsymbol{r}')\boldsymbol{F}_i(\boldsymbol{r}')\,dS'. \tag{5}$$

Above, Ω_i^c is the complement of Ω_i, i.e., the region outside Ω_i excluding the surface, and $\boldsymbol{F}_i(\boldsymbol{r}')$ is the electric or magnetic surface current. The integral operators including differentiation should be interpreted in the Cauchy principal value sense if the field point is on the surface. Function G_i represents the fundamental solution of the scalar Helmholtz equation in 3D corresponding to the homogeneous (source-free) problem associated with region i; that is,

$$G_i(\boldsymbol{r},\boldsymbol{r}') = \frac{e^{-jk_iR}}{4\pi R},\ R = |\boldsymbol{r}-\boldsymbol{r}'|, \tag{6}$$

where constant k_i designates the wave number of medium i, occupying region i, and defined as $k_i = \sqrt{\epsilon_i\mu_i}$. The fields $\boldsymbol{E}_i$ and $\boldsymbol{H}_i$ given by (2) and (3), satisfy source-free Maxwell's equations in Ω_i, and on the interface $\partial\Omega$ they are subject to the tangential boundary conditions

$$\gamma_t\boldsymbol{E}_1 = \gamma_t\boldsymbol{E}_2 \quad\text{and}\quad \gamma_t\boldsymbol{H}_1 = \gamma_t\boldsymbol{H}_2. \tag{7}$$

Here, the tangential trace operator γ_t acts on an arbitrary vector function $\boldsymbol{X}$ as

$$\gamma_t\boldsymbol{X} = -\hat{\boldsymbol{n}}\times\hat{\boldsymbol{n}}\times\boldsymbol{X}|_{\partial\Omega}, \tag{8}$$

and $\hat{\boldsymbol{n}}$ is the unit normal vector on $\partial\Omega$ pointing outwards (from region 2 to region 1). Substituting field representations (2) and (3) into (7), with appropriate trace theorems, results in the following equations,

$$\eta_1\gamma_t\mathcal{T}^1[\boldsymbol{J}_1](\boldsymbol{r}) - \eta_2\gamma_t\mathcal{T}^2[\boldsymbol{J}_2](\boldsymbol{r}) - \gamma_t\mathcal{K}^1[\boldsymbol{M}_1](\boldsymbol{r}) + \gamma_t\mathcal{K}^2[\boldsymbol{M}_2](\boldsymbol{r}) = -\boldsymbol{E}_1^{\mathrm{inc}}(\boldsymbol{r}), \quad \boldsymbol{r}\in\partial\Omega, \tag{9}$$

$$\frac{1}{\eta_1}\gamma_t\mathcal{T}^1[\boldsymbol{M}_1](\boldsymbol{r}) + \frac{1}{\eta_2}\gamma_t\mathcal{T}^2[\boldsymbol{M}_2](\boldsymbol{r}) - \gamma_t\mathcal{K}^1[\boldsymbol{J}_1]\boldsymbol{r} - \gamma_t\mathcal{K}^2[\boldsymbol{J}_2](\boldsymbol{r}) = -\boldsymbol{H}_1^{\mathrm{inc}}(\boldsymbol{r}), \quad \boldsymbol{r}\in\partial\Omega, \tag{10}$$

known as the PMCHWT integral equation formulation [18]. Here, due to the interface conditions, the surface currents satisfy $\boldsymbol{J}_1 = -\boldsymbol{J}_2$ and $\boldsymbol{M}_1 = -\boldsymbol{M}_2$. To summarize, we note that the original problem of finding the electromagnetic fields $\boldsymbol{E}_i$ and $\boldsymbol{H}_i$ everywhere outside and inside the particle is reformulated as SIEs for the equivalent surface current densities. Once these currents are found they can be used to evaluate the scattered electromagnetic fields everywhere in space. These fields, in turn, can be used to determine, e.g., the scattering and absorption efficiency of the particle.

B. Discretization strategy

In a usual MoM strategy, the surface of the target is partitioned into N_t triangular elements and the unknown currents are expanded with the set of known subsectional basis functions with the local support on the mesh. In this work, we approximate the currents with two subsets resulting from the hierarchical decomposition of the space spanned by triangle-based monopolar-RWG set ($\boldsymbol{m}_n$) [53], namely even monopolar-RWG subset ($\boldsymbol{m}_n^e$) and odd monopolar-RWG subset ($\boldsymbol{m}_n^o$) [54]. Even and odd monopolar-RWG basis functions are edge-based and defined on two triangles ($S_n^1 \cup S_n^2$) sharing the nth edge (l_n) as follows:

$$\boldsymbol{m}_n^e(\boldsymbol{r}') = \begin{cases} \frac{1}{2A_n^1}\left(\boldsymbol{r}'-\boldsymbol{r}_n^1\right), & \boldsymbol{r}'\in S_n^1, \\ -\frac{1}{2A_n^2}\left(\boldsymbol{r}'-\boldsymbol{r}_n^2\right), & \boldsymbol{r}'\in S_n^2, \end{cases} \tag{11}$$

$$\boldsymbol{m}_n^o(\boldsymbol{r}') = \begin{cases} \frac{1}{2A_n^1}\left(\boldsymbol{r}'-\boldsymbol{r}_n^1\right), & \boldsymbol{r}'\in S_n^1, \\ \frac{1}{2A_n^2}\left(\boldsymbol{r}'-\boldsymbol{r}_n^2\right), & \boldsymbol{r}'\in S_n^2, \end{cases} \tag{12}$$

$$1 \leqslant n \leqslant N_e,$$

where A_n^1 and A_n^2 denote the areas of the corresponding edge-adjacent triangles, S_n^1 and S_n^2, respectively (see Fig. 2). The position vectors of the free vertices opposite to the nth edge are designated by $\boldsymbol{r}_n^1$ and $\boldsymbol{r}_n^2$, and N_e is the number of edges in the mesh of the surface. According to (11) and Fig. 2, the even monopolar-RWG subset can be interpreted as a RWG set without the edge normalization because it maintains the continuity of the normal component of the current across the edges. On the other hand, in light of Eq. (12), the odd monopolar-RWG subset enforces the normal component of the current on both sides of the common edge to have the same absolute value but the opposite sign (see Fig. 2).

We approximate the unknown equivalent electric and magnetic currents, $\boldsymbol{J}_i$ and $\boldsymbol{M}_i$, over the two sides of the

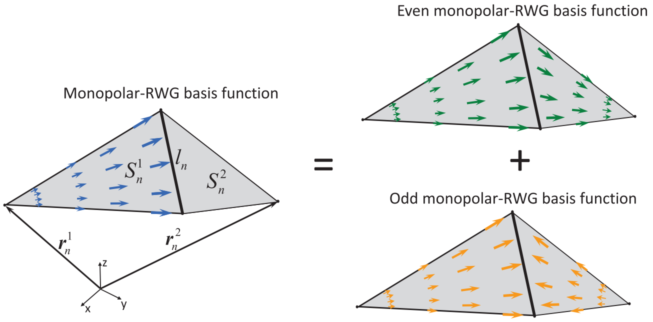

FIG. 2. Hierarchical decomposition of the triangle-based discontinuous monopolar-RWG set in terms of the edge-based even-monopolar-RWG subset and the odd-monopolar-RWG subset.

boundary of a plasmonic target ($i = 1, 2$) with the even and odd monopolar-RWG subsets as follows [41]:

$$\boldsymbol{J}_i(\boldsymbol{r}') \approx \sum_{n=1}^{2N_e} J_n^i \boldsymbol{m}_n = \sum_{n=1}^{N_e} a_n^{i,e} \boldsymbol{m}_n^e + \sum_{n=1}^{N_e} a_n^{i,o} \boldsymbol{m}_n^o, \tag{13}$$

$$\boldsymbol{M}_i(\boldsymbol{r}') \approx \sum_{n=1}^{2N_e} M_n^i \boldsymbol{m}_n = \sum_{n=1}^{N_e} b_n^{i,e} \boldsymbol{m}_n^e + \sum_{n=1}^{N_e} b_n^{i,o} \boldsymbol{m}_n^o, \tag{14}$$

where the sequences $\{J_n^i\} = \{a_n^{i,e}, a_n^{i,o}\}$ and $\{M_n^i\} = \{b_n^{i,e}, b_n^{i,o}\}$ represent the sets of unknown coefficients in the expansion of the currents. In view of expressions (13) and (14), our nonconforming implementation defines two basis functions for each mesh edge, thus leading to twice the number of degrees of freedom compared to the standard RWG expansion, which defines one basis function per edge. The approximated scattered electric and magnetic fields generated by the even and odd monopolar-RWG subsets yield

$$\tilde{\boldsymbol{E}}_i^{s,e/o} = \sum_{n=1}^{N_e} \eta_i \mathcal{T}_n^{i,e/o} a_n^{i,e/o} - \sum_{n=1}^{N_e} \mathcal{K}_n^{i,e/o} b_n^{i,e/o}, \tag{15}$$

$$\tilde{\boldsymbol{H}}_i^{s,e/o} = \sum_{n=1}^{N_e} \mathcal{K}_n^{i,e/o} a_n^{i,e/o} + \sum_{n=1}^{N_e} \frac{1}{\eta_i} \mathcal{T}_n^{i,e/o} b_n^{i,e/o}, \tag{16}$$

with associated integral operators defined as

$$\mathcal{K}_n^{i,e/o}(\boldsymbol{r}) = \nabla \times \iint_{S_n^1 \cup S_n^2} G_i(\boldsymbol{r}, \boldsymbol{r}') \boldsymbol{m}_n^{e/o}(\boldsymbol{r}') dS', \tag{17}$$

$$\mathcal{T}_n^{i,e/o}(\boldsymbol{r}) = \frac{1}{jk_i} \left(\nabla\nabla \cdot \iint_{S_n^1 \cup S_n^2} G_i(\boldsymbol{r}, \boldsymbol{r}') \boldsymbol{m}_n^{e/o}(\boldsymbol{r}') dS' + k_i^2 \iint_{S_n^1 \cup S_n^2} G_i(\boldsymbol{r}, \boldsymbol{r}') \boldsymbol{m}_n^{e/o}(\boldsymbol{r}') dS' \right). \tag{18}$$

The even-odd (EO) monopolar-RWG function discretized PMCHWT formulation imposes the tangential electric and magnetic field boundary conditions over the meshed boundary of the target $\tilde{S} = \bigcup_{t=1}^{N_t} S_t$ as follows:

$$\sum_{n=1}^{N_e} \gamma_t \left(\eta_1 \mathcal{T}_n^1 + \eta_2 \mathcal{T}_n^2 \right)_{\tilde{S}}^{e/o} a_n^{e/o} - \sum_{n=1}^{N_e} \gamma_t \left(\mathcal{K}_n^1 + \mathcal{K}_n^2 \right)_{\tilde{S}}^{e/o} b_n^{e/o} \approx -\gamma_t \boldsymbol{E}_{\tilde{S}}^{\text{inc}}, \tag{19}$$

$$\sum_{n=1}^{N_e} \gamma_t \left(\mathcal{K}_n^1 + \mathcal{K}_n^2 \right)_{\tilde{S}}^{e/o} a_n^{e/o} + \sum_{n=1}^{N_e} \gamma_t \left(\frac{1}{\eta_1} \mathcal{T}_n^1 + \frac{1}{\eta_2} \mathcal{T}_n^2 \right)_{\tilde{S}}^{e/o} b_n^{e/o} \approx -\gamma_t \boldsymbol{H}_{\tilde{S}}^{\text{inc}}, \tag{20}$$

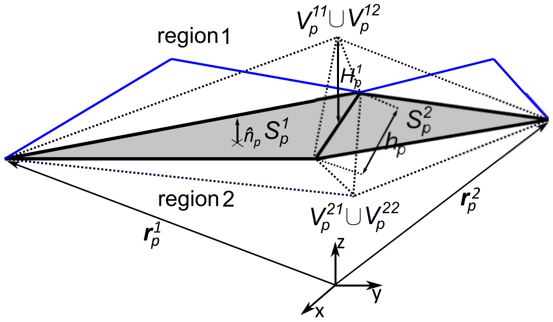

FIG. 3. Odd monopolar volumetric testing functions defined over a pair of facet-adjacent tetrahedra attached to the corresponding triangular facets and defined inside the region 1 (free-space) and region 2 (plasmonic nanoparticle).

where $a_n^{e/o} = a_n^{1,e/o} = -a_n^{2,e/o}$ and $b_n^{e/o} = b_n^{1,e/o} = -b_n^{2,e/o}$ is assumed such that the continuity of the surface currents is satisfied. We cast the discretized equations (19) and (20) into a matrix form by means of testing the tangential fields with an appropriate set of testing functions. The standard Galerkin MoM procedure, which adopts the same set for testing the fields and for the expansion of the unknown currents, leads to the following statements:

$$\iint_{S_p^1 \cup S_p^2} \left(\tilde{\boldsymbol{E}}_1^{s,e/o} - \tilde{\boldsymbol{E}}_2^{s,e/o} \right) \cdot \boldsymbol{m}_p^{e/o} dS = -\iint_{S_p^1 \cup S_p^2} \boldsymbol{E}^{\text{inc}} \cdot \boldsymbol{m}_p^{e/o} dS, \tag{21}$$

$$\iint_{S_p^1 \cup S_p^2} \left(\tilde{\boldsymbol{H}}_1^{s,e/o} - \tilde{\boldsymbol{H}}_2^{s,e/o} \right) \cdot \boldsymbol{m}_p^{e/o} dS = -\iint_{S_p^1 \cup S_p^2} \boldsymbol{H}^{\text{inc}} \cdot \boldsymbol{m}_p^{e/o} dS, \quad 1 \leqslant p \leqslant N_e. \tag{22}$$

Since the odd monopolar-RWG functions are not divergence-conforming, moving the gradients to the basis and testing functions in the testing of the $\mathcal{T}_n^{i,e/o}$ operator leads to double-contour strongly singular integrals that are not integrable in the Cauchy principal value sense. In fact, these integrals become unbounded for self- or edge-adjacent interactions. In this work, we circumvent this problem by the introduction of volumetric non-Galerkin testing scheme defined over a pair of facet-adjacent tetrahedral elements attached to the corresponding edge-adjacent triangles originating from the tessellation of the boundary (see Fig. 3). The testing elements are confined inside the region where, in accordance with the surface equivalence theorem, the fields must be zero [41]. These odd monopolar volumetric testing functions [41] $\{\boldsymbol{M}_p^{i,o}\}$ are designed to best couple with odd monopolar-RWG basis functions. They are defined over two facet-adjacent tetrahedral elements as follows:

$$\boldsymbol{M}_p^{i,o}(\boldsymbol{r}) = \begin{cases} \frac{1}{3v_p^{i,1}} \left(\boldsymbol{r} - \boldsymbol{r}_p^1 \right), & \boldsymbol{r} \in V_p^{i,1}, \\ \frac{1}{3v_p^{i,2}} \left(\boldsymbol{r} - \boldsymbol{r}_p^2 \right), & \boldsymbol{r} \in V_p^{i,2}. \end{cases} \tag{23}$$

Here, $v_p^{i,1}$ and $v_p^{i,2}$ stand for the volumes of the facet-adjacent tetrahedrons $V_p^{i,1}$ and $V_p^{i,2}$ attached to the boundary, lying in the region i and sharing the pth mesh edge.

We define the discretized EO-monopolar-RWG PMCHWT equations directly from expressions (21) and (22) by keeping the even surface testing and interchanging the odd surface testing with odd volumetric testing strategy. The odd volumetrically tested components of the matrix equation now become

$$\iiint_{V_p^{2,1}\cup V_p^{2,2}} \tilde{\boldsymbol{E}}_1^{s,e/o}\cdot \boldsymbol{M}_p^{2,o}dV - \iiint_{V_p^{1,1}\cup V_p^{1,2}} \tilde{\boldsymbol{E}}_2^{s,e/o}\cdot \boldsymbol{M}_p^{1,o}dV = -\iiint_{V_p^{2,1}\cup V_p^{2,2}} \boldsymbol{E}^{\mathrm{inc}}\cdot \boldsymbol{M}_p^{2,o}dV, \qquad (24)$$

$$\iiint_{V_p^{2,1}\cup V_p^{2,2}} \tilde{\boldsymbol{H}}_1^{s,e/o}\cdot \boldsymbol{M}_p^{2,o}dV - \iiint_{V_p^{1,1}\cup V_p^{1,2}} \tilde{\boldsymbol{H}}_2^{s,e/o}\cdot \boldsymbol{M}_p^{1,o}dV = -\iiint_{V_p^{2,1}\cup V_p^{2,2}} \boldsymbol{H}^{\mathrm{inc}}\cdot \boldsymbol{M}_p^{2,o}dV, \quad 1 \leqslant p \leqslant N_e. \qquad (25)$$

C. Numerical implementation

There are a couple of important points related to the numerical implementation of the proposed nonconforming discretization technique. First, special care has to be taken when defining the geometry of volumetric-testing elements near sharp wedges and corners since they may break out of the null-field region and numerical error may appear (see Fig. 3). In this work we define their geometry *conformal* to the boundary [40] taking into account the angles formed by the corresponding field triangle originating from the surface tessellation and the three neighboring triangles. The accuracy of this implementation can be fine-tuned by adjusting the height of the testing tetrahedral elements (H_p) which in turn is defined with the same value in both regions as a fraction of the length of the pth edge, h_p, shared by the corresponding field triangles where the volumetric elements are constructed.

Another important point is that in order to minimize the number of degrees of freedom, and maintain accuracy similar to that in the EO-monopolar-RWG approach, we use the *hybrid* version of the EO-monopolar-RWG discretization scheme of the PMCHWT formulation, EO-PMCHWT[hyb]. This scheme assumes the odd monopolar expansion of the currents and the volumetric testing of the fields just over the edges forming the physical sharp wedges and corners, and the conventional RWG expansion of the currents and testing of the fields over all the edges arising from the discretization. Therefore, for a given discretization, this formulation handles a number of degrees of freedom comparable to the RWG-PMCHWT strategy, PMCHWT[R].

In the nonconforming EO-PMCHWT[hyb] scheme, we compute the volumetric integrals over tetrahedra with 11-point cubature rules. The surface and line integrals are computed with a 9-point quadrature rule and the quasisingular contributions of the kernel are computed analytically for the inner integrals of all the interactions. In the RWG-PMCHWT implementation, the quasisingular kernel contributions are computed analytically for inner integrals and near interactions only, while the far interaction integrals are computed directly with a 4-point rule.

III. NUMERICAL RESULTS

We present numerical results of the scattering analysis of three sharp-edged plasmonic nanoparticles, namely, a hexahedron, an octahedron, and a tetrahedron, discretized with geometrically conformal meshes in which adjacent triangles share the same edge. We choose such particles since their modeling is especially convoluted due to the singular field behavior induced near sharp edges and corners. In addition, for these particles, the redshift (resonances shift to the higher wavelengths) in scattering and absorption spectra and the improvements in the near field computed with our nonconforming EO-PMCHWT[hyb] implementation when compared to the PMCHWT[R] implementation are especially evident. In all examples, the incident plane wave is x-polarized, propagating from the $+z$ direction, and the currents are computed through the direct solution of the resulting linear system. All particles analyzed here are of equal volume ($V = 50^3$ nm^3).

A. Scattering and absorption spectra in resonance domain

We focus on scattering and absorption spectra around two main resonances. For all three particles, we present three

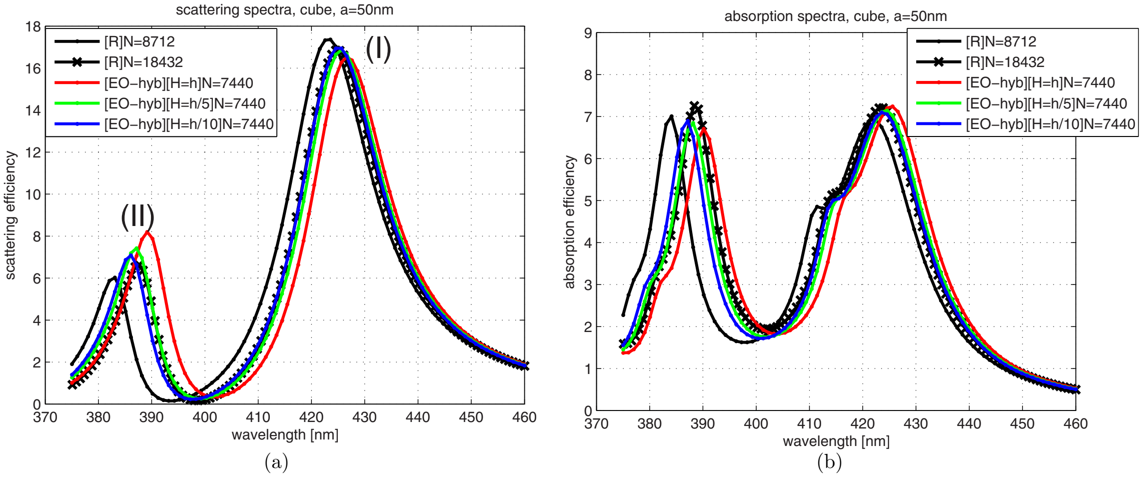

(a) (b)

FIG. 4. Scattering (a) and absorption (b) spectra for a hexahedron (cube) with edge length $a = 50$ nm. The first resonance (I) exposes strong coupling with the incident field (scattering efficiency ≈17). Resonance (II) shows moderate scattering amplitude (scattering efficiency ≈7), but the absorption maximum is about the same magnitude as with the first resonance.

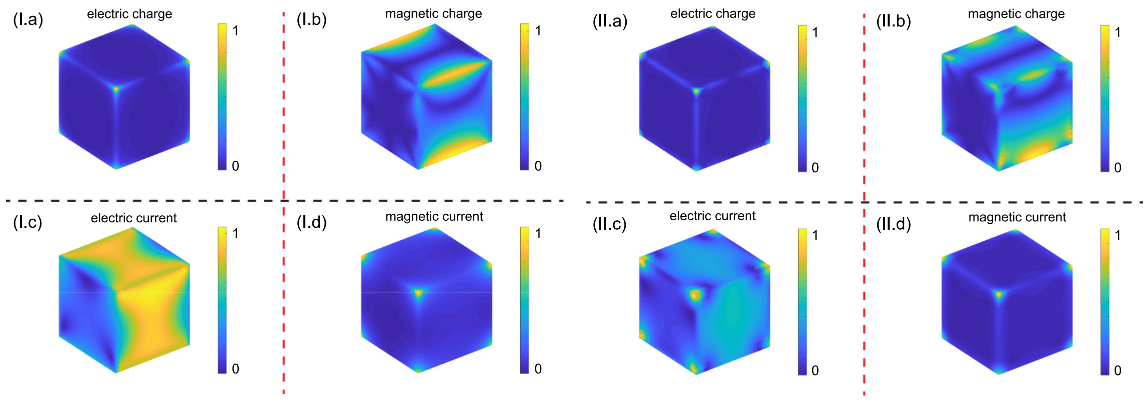

(a) (b)

FIG. 5. Normalized absolute values of electric and magnetic charges and currents around dipole (I) and quadrupole (II) resonances for a cube with edge length $a = 50$ nm. The colors indicate minimum (blue) to maximum (yellow) normalized charge and current values. Electric charge densities [(I.a) and (II.a)] and magnetic current densities [(I.d) and (II.d)] exhibit extremely singular nature around corners for both resonances.

different sets of results. First, we compute the resonant efficiencies with our nonconforming EO-PMCHWT[hyb] implementation and several values of the heights of the testing elements H to illustrate the effect of H on the accuracy of the results. We compare these results to the ones computed with the PMCHWT[R] discretization technique. Next, we plot the equivalent electric and magnetic surface charges and currents for the first two resonances, indicating the strongly singular behavior over the sharp edges and corners of the particle. Finally, a comparative convergence plot of the main resonant peaks is presented, illuminating further the achieved enhancement of the proposed new discretization technique versus the standard scheme. The scattering and absorption efficiencies are computed directly from the surface currents and MoM matrices according to the expressions given in [55]. All the meshes used in the computation of scattering and absorption spectra are structured without h refinements.

1. Plasmonic hexahedron (cube)

The electromagnetic response of a hexahedron, or commonly known as the cube, has been studied intensively during the last 50 years (see [36] and references therein). From Fig. 4 we can notice the redshift of the first (dipole) and second (quadrupole) resonances obtained with nonconforming EO-PMCHWT[hyb] and $N = 7440$ unknowns when compared to the resonances obtained with PMCHWT[R] and $N = 8712$ unknowns for both electric and magnetic currents. Furthermore, for the best performing H, where the height of testing elements is equal to the mesh parameter, $H = h$, the observed redshift is even more pronounced, surpassing the spectra computed with PMCHWT[R] and 18 432 unknowns. In Fig. 5 we can notice singular surface currents and charges around sharp corners. In particular, the surface electric charge density and surface magnetic current density show extremely singular nature around sharp vertices for both resonances. In Fig. 6 we show the convergence trends of the resonant wavelengths

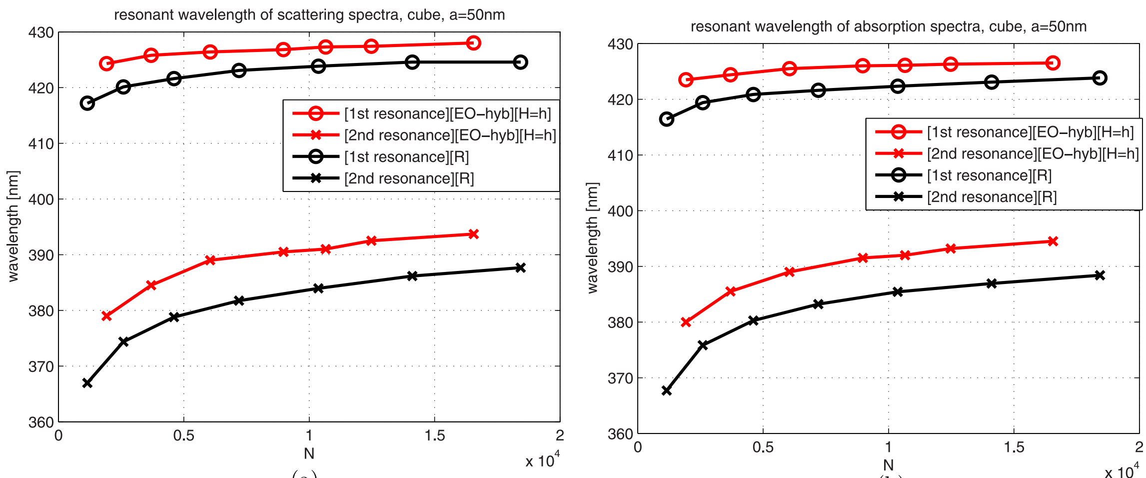

(a) (b)

FIG. 6. Convergence of the resonant wavelengths of two main resonances in scattering spectra (a) and absorption spectra (b) versus the number of degrees of freedom for the same hexahedron inclusion as in Fig. 4.

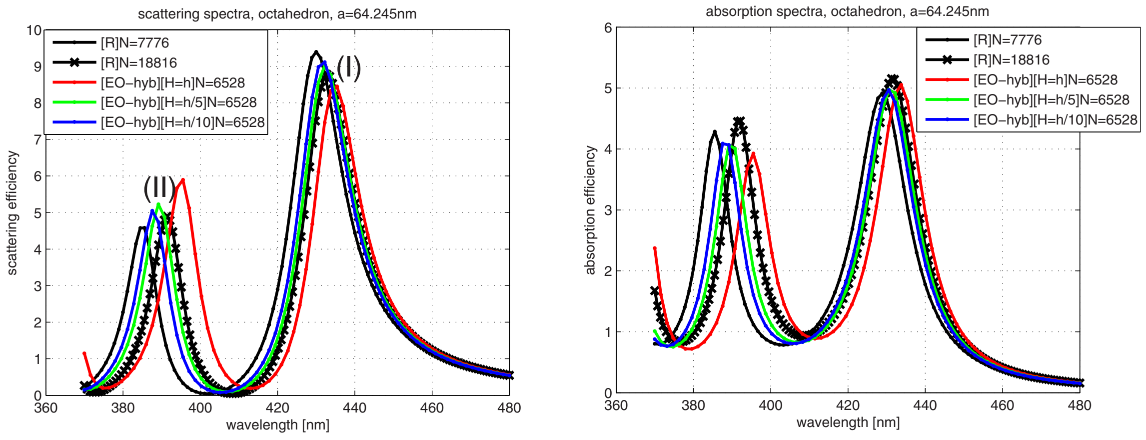

(a) (b)

FIG. 7. Scattering (a) and absorption (b) efficiency spectra for the octahedral inclusion of edge length $a = 64.245$ nm. In this case the maximum scattering and absorption efficiency values are close to 10 and 5, respectively.

for the first two resonances in the scattering and absorption spectra, respectively, versus the number of degrees of freedom N. The results are computed with the EO-PMCHWT[hyb] and best performing H and compared to the results computed with the standard PMCHWT[R] discretization. Our nonconforming scheme exhibits faster convergence of resonant wavelengths compared to the RWG implementation when the number of unknowns is increased. In particular, the dipole and quadrupole resonances computed with our nonconforming scheme, and $H = h$, have been marked around the incident wavelengths of 428 nm and 393 nm, respectively, using around 16 560 unknowns for the electric and magnetic currents (see Fig. 6).

2. Plasmonic octahedron

The octahedron has the dual shape of the cube and the solid angle sharper than the cube, however, smoother than the one of the tetrahedron [36]. Therefore, we expect that its two main resonances are going to be redshifted when compared to the cube, but blueshifted (shifted to lower wavelengths) when compared to the tetrahedron [36]. Similarly to the cube, the redshift of the two main resonances computed with EO-PMCHWT[hyb] and different values of H with $N = 6528$ degrees of freedom compared to the resonances computed with PMCHWT[R] and $N = 7776$ degrees of freedom is recognized in Fig. 7. In light of Fig. 8, a strong concentration of surface field quantities is found around sharp corners.

The two resonances cannot be distinguished solely by looking in electric charge and magnetic current distributions because they are too singular and concentrated around vertices. However, the surface magnetic charge and electric current distributions reveal the different nature of the dipole and quadrupole resonances. Furthermore, in view of Fig. 9, faster convergence of the resonant wavelengths computed with EO-PMCHWT[hyb] and $H = h$ when compared to the resonant wavelengths computed with PMCHWT[R] is observed when the number of unknowns is increased. We were

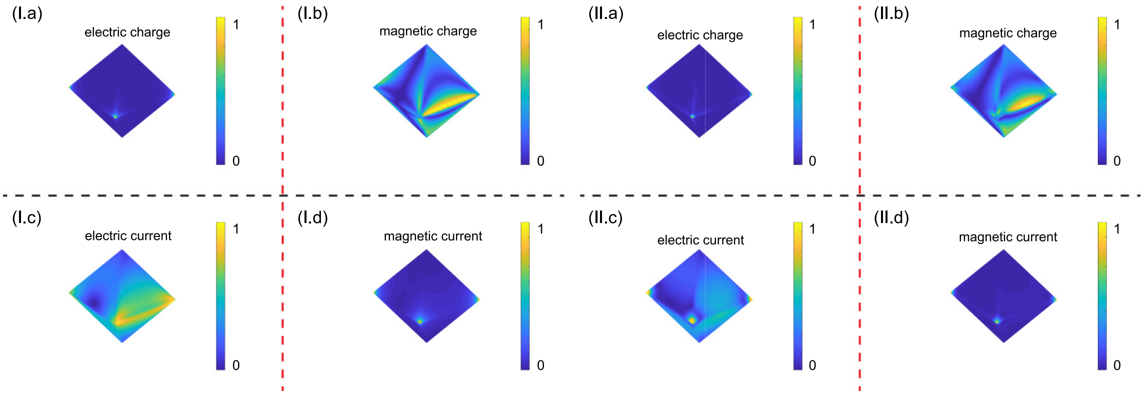

(a) (b)

FIG. 8. Normalized absolute values of electric and magnetic charges and currents around two main resonances for an octahedron with edge length $a = 64.245$ nm. Similarly to the cube, we notice strong singular field quantities induced near sharp edges and corners. The two resonances can be distinguished by looking at the surface magnetic charge and electric current distributions.

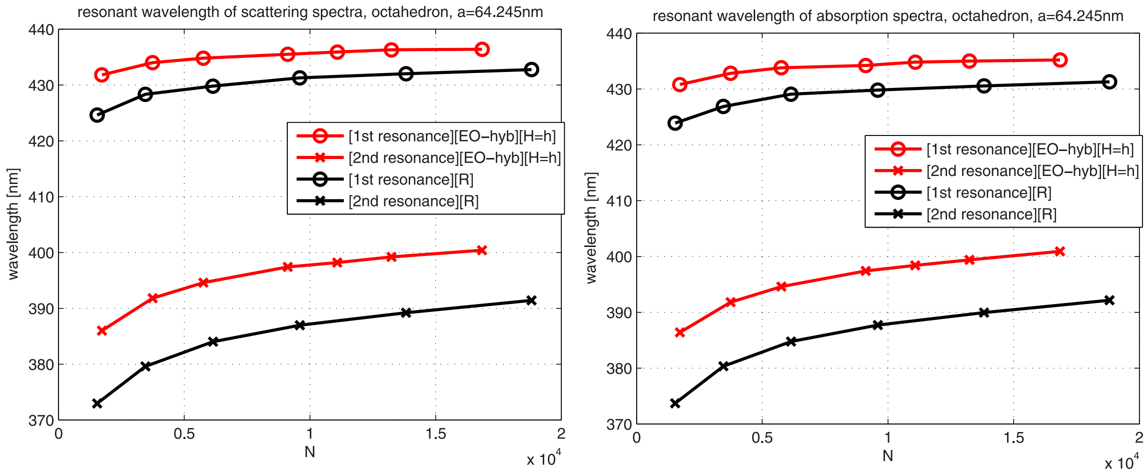

(a) (b)

FIG. 9. Convergence of the resonant wavelengths of two main resonances versus the number of degrees of freedom for the scattering (a) and absorption (b) efficiency of the octahedral inclusion. The EO-PMCHWT[hyb] scheme indicates faster convergence with respect to the standard RWG discretization scheme.

able to spot the resonant wavelengths of the first and second resonances around 436 nm and 400 nm, respectively, with our nonconforming implementation and around 16 840 degrees of freedom for the electric and magnetic currents (see Fig. 9).

3. *Plasmonic tetrahedron*

The tetrahedron is the sharpest member of the Platonic solids and its plasmonic resonances are redshifted compared to the other members [36]. In view of Fig. 10, we can notice the redshift of the scattering and absorption spectra computed with our nonconforming implementations and $N = 4104$ unknowns with respect to the RWG implementation and $N = 4800$ unknowns. Similarly to the cube and the octahedron, strong singular fields are present near sharp features of the particle (Fig. 11). Again, the two resonances are indistinguishable from the plots of surface electric charge and magnetic current since they are focused near sharp vertices. Instead, one should look at the surface magnetic charge and electric current distributions, which show a distinct nature for a particular resonance. According to Fig. 12, we can detect faster convergence of the resonant wavelengths computed with EO-PMCHWT[hyb] when compared to the resonant wavelengths computed with PMCHWT[R] as the number of degrees of freedom is increased. In particular, we were able to spot the first and second resonance in the scattering and absorption spectra around the incident wavelengths of 565 nm and 490 nm, respectively, using our EO-PMCHWT[hyb] implementation with $H = h$ and around 16 000 unknowns for the electric and magnetic currents (see Fig. 12).

B. Near-field computations in resonance domain

The results of the previous section indicate that faster convergence in the far-field region can be obtained with

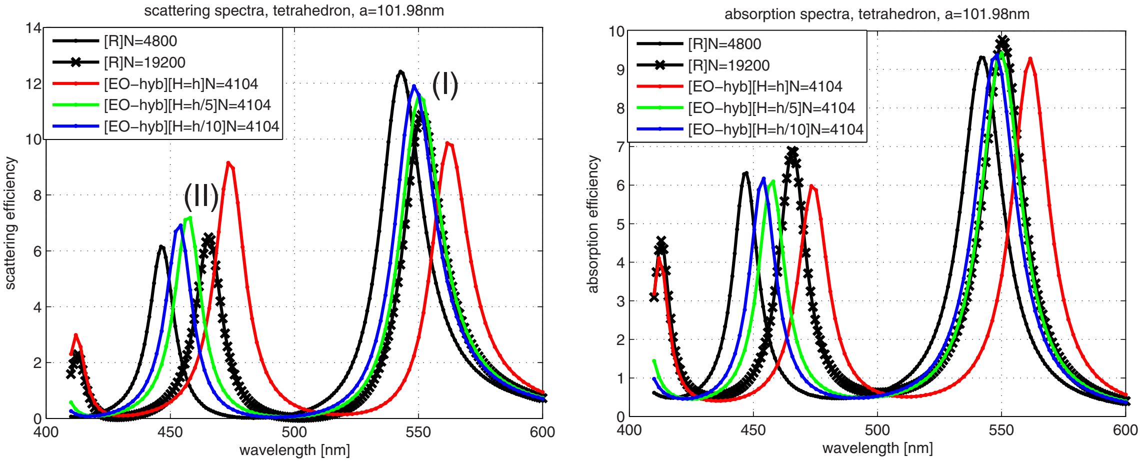

(a) (b)

FIG. 10. The scattering (a) and absorption (b) efficiency spectra for the tetrahedral particle of edge length $a = 101.98$ nm depicting the first two resonances. We can spot the maximum scattering and absorption efficiency values around 12 and 10, respectively.

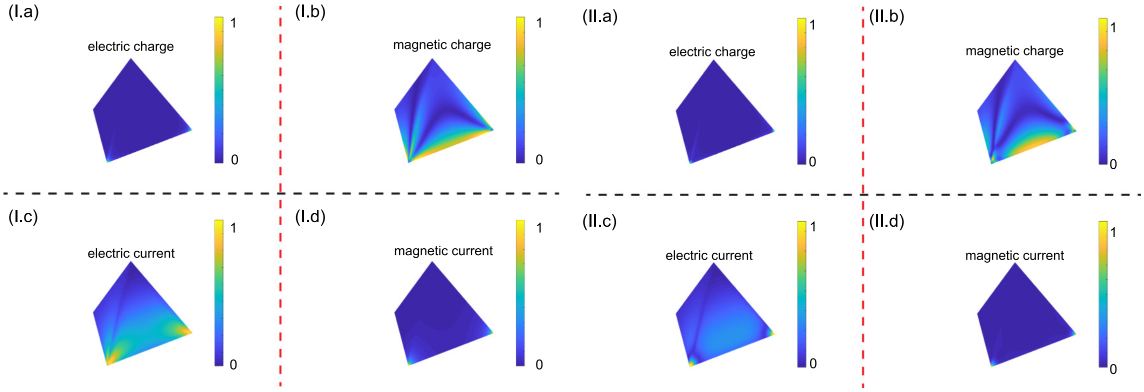

FIG. 11. Normalized absolute values of electric and magnetic charges and currents around first (I) and second (II) resonances for a tetrahedron with edge length $a = 101.98$ nm. Very strong singular behavior of surface electric charge and magnetic current densities is visible near the sharp vertices.

the proposed EO-PMCHWT[hyb] scheme than with PMCHWT[R]. Next, we test the near-field accuracy of our EO-PMCHWT[hyb] formulation around two main resonances in the scattering spectra of a plasmonic cube with edge length $a = 50$ nm. For this purpose, we define the root-mean-square (rms) near-field relative error e_{near} as follows [40]:

$$e_{\text{near}} = \frac{\left[\sum_{j=1}^{K} \left|\tilde{\boldsymbol{E}}_s(\boldsymbol{r}_j) - \boldsymbol{E}_s^{\text{REF}}(\boldsymbol{r}_j)\right|^2 + \eta_0^2 \sum_{j=1}^{K} \left|\tilde{\boldsymbol{H}}_s(\boldsymbol{r}_j) - \boldsymbol{H}_s^{\text{REF}}(\boldsymbol{r}_j)\right|^2\right]^{1/2}}{\left[\sum_{j=1}^{K} \left|\boldsymbol{E}_s^{\text{REF}}(\boldsymbol{r}_j)\right|^2 + \eta_0^2 \sum_{j=1}^{K} \left|\boldsymbol{H}_s^{\text{REF}}(\boldsymbol{r}_j)\right|^2\right]^{1/2}}, \tag{26}$$

where $\tilde{\boldsymbol{E}}_s$ and $\tilde{\boldsymbol{H}}_s$ denote the scattered electric and magnetic fields, respectively, computed with the EO-PMCHWT[hyb] or PMCHWT[R] implementation. The reference scattered fields, $\boldsymbol{E}_s^{\text{REF}}$ and $\boldsymbol{H}_s^{\text{REF}}$, are computed with the standard PMCHWT[R] implementation on an unstructured mesh with h refinement around sharp edges and corners and the maximum number of degrees of freedom (18 432) for the electric and magnetic currents. The near fields are computed on a set of K points distributed along the line with length 100 nm defined 2.5 nm above the edge of the cube [see Fig. 13(a)]. In our experiment, we adopt $K = 200$ and the fields $\tilde{\boldsymbol{E}}_s$ and $\tilde{\boldsymbol{H}}_s$ are computed using a structured mesh without h refinement.

In Fig. 13(b) we show the relative rms near-field errors versus the number of degrees of freedom N computed with EO-PMCHWT[hyb] ($H = h$) and PMCHWT[R] implementations. In light of Fig. 13(b), we can observe smaller near-field errors obtained with the EO-PMCHWT[hyb] scheme and fewer numbers of unknowns when compared to PMCHWT[R].

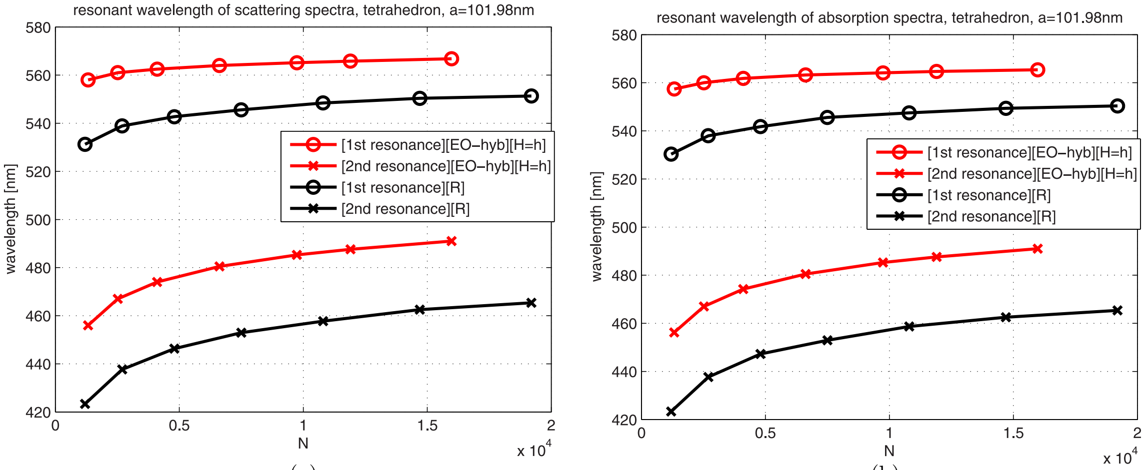

(a) (b)

FIG. 12. Convergence of the resonant wavelengths of two main resonances in scattering (a) and absorption (b) efficiency spectra versus the number of degrees of freedom for the same tetrahedron as in Fig. 10.

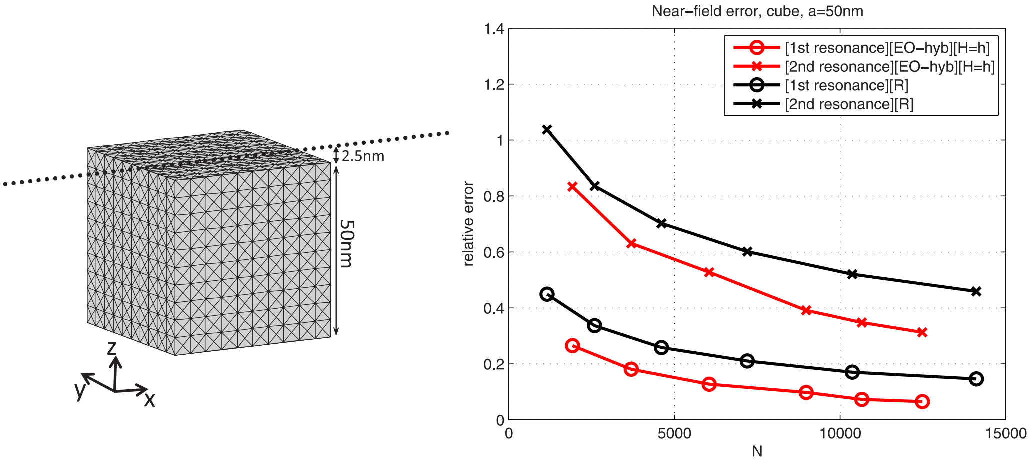

(a) (b)

FIG. 13. (a) Distribution of the points near a plasmonic cube, above one of the edges, that are used in the near-field accuracy tests. (b) Near-field relative error at the first and second resonances computed with the nonconforming [EO-hyb] and standard [R] implementations versus the number of degrees of freedom N for a plasmonic cube with side $a = 50$ nm.

IV. CONCLUSIONS

We have introduced a nonconforming discontinuous method of moments discretization of the PMCHWT integral equation formulation applied to the scattering analysis of plasmonic subwavelength nanoparticles with sharp vertices in their resonance domain. Following the recently introduced discretization strategy [41], the unknown electric and magnetic surface current densities are expanded with edge-based even and odd monopolar-RWG subsets, which stand for a hierarchical rearrangement of the monopolar-RWG set. To make the problematic singular kernel contributions numerically manageable, the fields are tested over pairs of small tetrahedral elements attached to the triangles on the boundary surface and lying in the null-field region.

The proposed technique appears to have improved performance features in the scattering analysis of plasmonic nanoparticles with sharp edges and corners. For these particles singular field quantities around geometric singularities dominate the physical result, creating a slow (or no) convergent solutions, particularly if standard discretization techniques are applied. The observed accuracy boost of the proposed implementation is attributed to the better singular charge and current modeling near the sharp edges and corners with a discontinuous expansion of the currents together with the volumetric testing of the fields close to the boundary of the target. The accuracy of our results was tested for both far-field and near-field characteristics, supporting an overall improvement in both domains.

In particular, we observe that the redshift in the scattering and absorption spectra around two main resonances, for the cases of canonical sharp-edged targets considered here, becomes more evident as the height of testing elements H increases up to the maximum value of the mesh parameter h. Additionally, we noticed a slower convergence of the second resonance compared to the resonant wavelength of the first resonance as the number of degrees of freedom increases. This indicates that the higher-order modes experience slower convergence than the lower-order ones.

Three different particles were purposefully presented in an increasing sharpness manner, i.e., the solid vertex for the cube is $\pi/2$ (rad), for the octahedron 1.359 (rad), and for the tetrahedron 0.551 (rad). With this categorization, we can deduce that the proposed nonconforming EO-PMCHWT[hyb] scheme exhibits faster convergence compared to the conventional PMCHWT[R] scheme as the solid vertex decreases, i.e., sharper particles. Alternatively, the sharper the solid, the less degrees of freedom are required for our nonconforming implementation to reach the same accuracy as with the standard RWG implementation. This fact can be of particular interest for modeling even sharper naturally or artificially occurring particles reducing at the same time the required mesh burden, paving the way towards the efficient computational exploration of the resonant physics and the design prospects of sharp nanoscatterers. The same methodology could also be utilized in incorporating quantum-corrected classical models that require a hybrid surface-volume treatment that captures electron tunneling and electron spill-out effects.

ACKNOWLEDGMENTS

This work was supported by FEDER and the Spanish Comisión Interministerial de Ciencia y Tecnologia (CICYT) under Projects No. TEC2013-47360-C3-1-P, No. TEC2016-78028-C3-1-P, and No. TEC2017-84817-C2-2-R and the Unidad de Excelencia Maria de Maeztu MDM-2016-0600, which is financed by the Agencia Estatal de Investigación, Spain.

[1] S. A. Maier, *Plasmonics: Fundamentals and Applications* (Springer, New York, 2007).
[2] K. L. Kelly, E. Coronado, L. L. Zhao, and G. C. Schatz, The optical properties of metal nanoparticles: The influence of size, shape, and dielectric environment, J. Phys. Chem. B **107**, 668 (2003).
[3] J. Homola, Surface plasmon resonance sensors for detection of chemical and biological species, Chem. Rev. **108**, 462 (2008).
[4] K. R. Catchpole and A. Polman, Plasmonic solar cells, Opt. Express **16**, 21793 (2008).
[5] J. A. Schuller, E. S. Barnard, W. Cai, Y. C. Jun, J. S. White, and M. L. Brongersma, Plasmonics for extreme light concentration and manipulation, Nat. Mater. **9**, 193 (2010).
[6] S. Kawata (ed.), *Near-Field Optics and Surface Plasmon Polaritons* (Springer, Berlin, 2014).
[7] A. L. González, C. Noguez, and A. S. Barnard, Map of the structural and optical properties of gold nanoparticles at thermal equilibrium, J. Phys. Chem. C **116**, 14170 (2012).
[8] M. Kauranen and A. V. Zayats, Nonlinear plasmonics, Nat. Photonics **6**, 737 (2012).
[9] X. Fan, W. Zheng, and D. J. Singh, Light scattering and surface plasmons on small spherical particles, Light Sci. Appl. **3**, e179 (2014).
[10] D. C. Tzarouchis, P. Ylä-Oijala, and A. Sihvola, Light scattering by a dielectric sphere: Perspectives on the Mie resonances, Appl. Sci. **8**, 184 (2018).
[11] I. Sosa, C. Noguez, and R. Barrera, Optical properties of metal nanoparticles with arbitrary shapes, J. Phys. Chem. B **107**, 6269 (2003).
[12] V. Amendola, O. Bakr, and F. Stellacci, A study of the surface plasmon resonance of silver nanoparticles by the discrete dipole approximation method: Effect of shape, size, structure, and assembly, Plasmonics **5**, 85 (2010).
[13] O. S. Vartia, P. Ylä-Oijala, J. Markkanen, S. Puupponen, A. Seppälä, A. Sihvola, and T. Ala-Nissila, On the applicability of discrete dipole approximation for plasmonic particles, J. Quant. Spectrosc. Radiat. Transfer **169**, 23 (2016).
[14] F. Hao and P. Nordlander, Efficient dielectric function for FDTD simulation of the optical properties of silver and gold nanoparticles, Chem. Phys. Lett. **446**, 115 (2007).
[15] I. D. Mayergoyz, D. R. Fredkin, and Z. Zhang, Electrostatic (plasmon) resonances in nanoparticles, Phys. Rev. B **72**, 155412 (2005).
[16] U. Hohenester and J. Krenn, Surface plasmon resonances of single and coupled metallic nanoparticles: A boundary integral method approach, Phys. Rev. B **72**, 195429 (2005).
[17] V. Myroshnychenko, J. Rodríguez-Fernández, I. Pastoriza-Santos, A. M. Funston, C. Novo, P. Mulvaney, L. M. Liz-Marzán, and F. J. García de Abajo, Modeling the optical response of gold nanoparticles, Chem. Soc. Rev. **37**, 1792 (2008).
[18] A. J. Poggio and E. K. Miller, Integral equation solutions of three-dimensional scattering problems, in *Computer Techniques for Electromagnetics*, edited by R. Mittra (Pergamon Press, Oxford, 1973).
[19] T. K. Wu and L. L. Tsai, Scattering from arbitrarily-shaped lossy dielectric bodies of revolution, Radio Sci. **12**, 709 (1977).
[20] Y. Chang and R. F. Harrington, A surface formulation for characteristic modes of material bodies, IEEE Trans. Antennas Propag. **25**, 789 (1977).
[21] A. M. Kern and O. J. F. Martin, Surface integral formulation for 3D simulations of plasmonic and high permittivity nanostructures, J. Opt. Soc. Am. A **26**, 732 (2009).
[22] M. G. Araújo, J. M. Taboada, D. M. Solís, J. Rivero, L. Landesa, and F. Obelleiro, Comparison of surface integral equation formulations for electromagnetic analysis of plasmonic nanoscatterers, Opt. Express **20**, 9161 (2012).
[23] C. Forestiere, G. Iadarola, G. Rubinacci, A. Tamburrino, L. Dal Negro, and G. Miano, Surface integral formulations for the design of plasmonic nanostructures, J. Opt. Soc. Am. A **29**, 2314 (2012).
[24] R. F. Harrington, *Field Computation by Moment Method* (Macmillan, New York, 1968).
[25] S. M. Rao, D. R. Wilton, and A. W. Glisson, Electromagnetic scattering by surfaces of arbitrary shape, IEEE Trans. Antennas Propag. **30**, 409 (1982).
[26] A. Buffa, R. Hiptmair, T. von Petersdorff, and C. Schawb, Boundary element methods for Maxwell transmission problems in Lipschitz domains, Numer. Math. **95**, 459 (2003).
[27] P. Ylä-Oijala, S. P. Kiminki, and S. Järvenpää, Conforming testing of electromagnetic surface integral equations for penetrable objects, IEEE Trans. Antennas Propag. **64**, 2348 (2016).
[28] M. Danckwerts and L. Novotny, Optical Frequency Mixing at Coupled Gold Nanoparticles, Phys. Rev. Lett. **98**, 026104 (2007).
[29] N. Grillet, D. Manchon, F. Bertorelle, C. Bonnet, M. Broyer, E. Cottancin, J. Lermé, M. Hillenkamp, and M. Pellarin, Plasmon coupling in silver nanocube dimers: Resonance splitting induced by edge rounding, ACS Nano **5**, 9450 (2011).
[30] J. Kern, S. Großmann, N. V. Tarakina, T. Häckel, M. Emmerling, M. Kamp, J. S. Huang, P. Biagioni, J. C. Prangsma, and B. Hecht, Atomic-scale confinement of resonant optical fields, Nano Lett. **12**, 5504 (2012).
[31] D. O. Sigle, J. Mertens, L. O. Herrmann, R. W. Bowman, S. Ithurria, B. Dubertret, Y. Shi, H. Y. Yang, C. Tserkezis, J. Aizpurua, and J. J. Baumberg, Monitoring morphological changes in 2D monolayer semiconductors using atom-thick plasmonic nanocavities, ACS Nano **9**, 825 (2015).
[32] M. Urbieta, M. Barbry, Y. Zhang, P. Koval, D. Sánchez-Portal, N. Zabala, and J. Aizpurua, Atomic-scale lightning rod effect in plasmonic picocavities: A classical view to a quantum effect, ACS Nano **12**, 585 (2018).
[33] L. C. Davis, Electrostatic edge modes of a dielectric wedge, Phys. Rev. B **14**, 5523 (1976).
[34] V. Klimov, G. Y. Guo, and M. Pikhota, Plasmon resonances in metal nanoparticles with sharp edges and vertices: A material independent approach, J. Phys. Chem. C **118**, 13052 (2014).
[35] D. C. Tzarouchis, P. Ylä-Oijala, T. Ala-Nissila, and A. Sihvola, Shape effects on surface plasmons in spherical, cubic, and rod-shaped silver nanoparticles, Appl. Phys. A **122**, 298 (2016).
[36] D. C. Tzarouchis, P. Ylä-Oijala, and A. Sihvola, Study of plasmonic resonances on Platonic solids, Radio Sci. **52**, 1450 (2017).
[37] R. D. Graglia and G. Lombardi, Singular higher order divergence conforming bases of additive kind and moments method applications to 3D sharp-wedge structures, IEEE Trans. Antennas Propag. **56**, 3768 (2008).
[38] J. Meixner, The behavior of electromagnetic fields at edges, IEEE Trans. Antennas Propag. **20**, 442 (1972).

[39] I. Sekulic, E. Ubeda, and J. M. Rius, Nonconforming discretization of the PMCHWT integral equation applied to arbitrarily shaped dielectric objects, in *2017 11th European Conference on Antennas and Propagation (EUCAP)* (IEEE, Paris, France, 2017), pp. 311–314.

[40] I. Sekulic, E. Ubeda, and J. M. Rius, Versatile and accurate schemes of discretization for the electromagnetic scattering analysis of arbitrarily shaped piecewise homogeneous objects, J. Comput. Phys. **374**, 478 (2018).

[41] E. Ubeda, I. Sekulic, and J. M. Rius, Hierarchical discretization of the PMCHWT formulation with jump current discontinuities for the scattering analysis of ferromagnetic objects, in *Proceedings of the International Conference on Electromagnetics in Advanced Applications (ICEAA)* (IEEE, Verona, Italy, 2017), p. 1093.

[42] R. Fuchs, Theory of the optical properties of ionic crystal cubes, Phys. Rev. B **11**, 1732 (1975).

[43] J. Avelin, A. N. Arslan, J. Brännback, M. Flykt, C. Icheln, J. Juntunen, K. Kärkkänen, T. Niemi, O. Nieminen, T. Tares, C. Toma, T. Uusitupa, and A. Sihvola, Electric fields in the source region: The depolarization dyadic for a cubic cavity, Electr. Eng. **81**, 199 (1998).

[44] J. P. Kottmann, O. J. F. Martin, D. R. Smith, and S. Schultz, Plasmon resonances of silver nanowires with a nonregular cross section, Phys. Rev. B **64**, 235402 (2001).

[45] A. Tao, P. Sinsermsuksakul, and P. Yang, Polyhedral silver nanocrystals with distinct scattering signatures, Angew. Chemie Int. Ed. **45**, 4597 (2006).

[46] S. Zhang, K. Bao, N. J. Halas, H. Xu, and P. Nordlander, Substrate-induced Fano resonances of a plasmonic nanocube: A route to increased-sensitivity localized surface plasmon resonance sensors revealed, Nano Lett. **11**, 1657 (2011).

[47] M. B. Cortie, F. Liu, M. D. Arnold, and Y. Niidome, Multimode resonances in silver nanocuboids, Langmuir **28**, 9103 (2012).

[48] L. Hung, S. Y. Lee, O. McGovern, O. Rabin, and I. Mayergoyz, Calculation and measurement of radiation corrections for plasmon resonances in nanoparticles, Phys. Rev. B **88**, 075424 (2013).

[49] M. J. Lagos, A. Trügler, U. Hohenester, and P. E. Batson, Mapping vibrational surface and bulk modes in a single nanocube, Nature (London, U.K.) **543**, 529 (2017).

[50] D. Ramaccia, S. Arcieri, A. Toscano, and F. Bilotti, Core-shell super-spherical nanoparticles for LSPR-based sensing platforms, IEEE J. Sel. Top. Quantum Electron. **23**, 1 (2017).

[51] U. Hohenester, Quantum corrected model for plasmonic nanoparticles: A boundary element method implementation, Phys. Rev. B **91**, 205436 (2015).

[52] H. Wallén, H. Kettunen, and A. Sihvola, Composite near-field superlens design using mixing formulas and simulations, Metamaterials **3**, 129 (2009).

[53] E. Ubeda and J. M. Rius, Novel monopolar MoM-MFIE discretization for the scattering analysis of small objects, IEEE Trans. Antennas Propag. **54**, 50 (2006).

[54] E. Ubeda, J. M. Rius, and A. Heldring, Nonconforming discretization of the electric-field integral equation for closed perfectly conducting objects, IEEE Trans. Antennas Propag. **62**, 4171 (2014).

[55] M. T. Homer Reid and S. G. Johnson, Efficient computation of power, force, and torque in BEM scattering calculations, IEEE Trans. Antennas Propag. **63**, 3588 (2015).